Advances in Geo-Energy Research

Vol. 19, No. 1, p. 30-42, 2026

Original article

Physically constrained intelligent interpretation of production profiles for multilayer oil wells based on distributed fiber optic temperature monitoring

Mingqiang Wei[1]*, Xue Chen[1], Xiyu Duan[2], Tao Zhang[1], Yingjie Wang[3], Hung Vo Thanh[4]

[1]*College of Petroleum and Natural Gas Engineering, Southwest Petroleum University, Chengdu 610500, P. R. China*

[2]*Shale Gas Research Institute, PetroChina Southwest Oil & Gasfield Company, Chengdu 610051, P. R. China*

[3]*China Petroleum Logging Co., Ltd. North China Branch, Cangzhou 061000, P. R. China*

[4]*Waseda Research Institute for Science and Engineering, Waseda University, Tokyo 169-855, Japan*

Keywords:
Multilayer oil wells
distributed temperature sensors
production profiles
intelligent interpretation

Cited as:
Wei, M., Chen, X., Duan, X., Zhang, T., Wang, Y., Vo Thanh, H. Physically constrained intelligent interpretation of production profiles for multilayer oil wells based on distributed fiber optic temperature monitoring. Advances in Geo-Energy Research, 2026, 19(1): 30-42. https://doi.org/10.46690/ager.2026.01.03

Abstract:
Distributed fiber optic temperature sensing provides significant advantages for production monitoring in complex geological environments due to its high precision, real-time capability, and long-term stability. However, its expanding application generates increasingly complex temperature datasets that challenge conventional production profile interpretation methods. To address these challenges, in this study, the researchers developed an intelligent interpretation framework to combine physically constrained forward modeling with data-driven machine learning techniques. A forward model of wellbore temperature profiles was established based on the fundamental principles of momentum conservation, energy conservation, and two-phase flow dynamics. Sensitivity analysis was used to identify key controlling factors, including production rate, geothermal gradient, reservoir thickness, crude oil heat capacity, and crude oil density, which were then used to generate representative training datasets. Three neural network architectures, including a fully connected neural network, a radial basis function network, and a back propagation network, were systematically trained and compared. The fully connected neural network demonstrated superior prediction accuracy and generalization capability, offering a robust tool for production profiling. Field validation using actual distributed fiber optic temperature-sensing monitoring data from commingled production wells confirmed the method's practical effectiveness, with predicted production rates strongly agreeing with the measured values across multiple reservoir layers. The proposed framework provides a reliable, efficient solution for interpreting the production profiles of multilayer wells under single-phase flow conditions. This study establishes a foundational methodology that can be extended to more complex multiphase flow scenarios in future research, thereby contributing to intelligent and automated reservoir management.

1. Introduction

Distributed temperature sensing (DTS) is widely employed in oilfields for production profile monitoring due to its high-precision, real-time capabilities (Denney, 2010). Although it has been increasingly applied to various downhole scenarios (Ekechukwu and Sharma, 2021), accurate interpretation of complex temperature data remains challenging (Lu et al., 2023), which has motivated researchers to continue developing predictive models for wellbore temperature distribution.

Yandy Scientific Press

*Corresponding author.
E-mail address: weiqiang425@163.com (M. Wei); Chenxue9928@163.com (X. Chen); duanxiyu007@gmail.com (X. Duan); tobiascheuing@163.com (T. Zhang); hbwangyj@cnpc.com.cn (Y. Wang); vothanhhung198090@gmail.com (H. Vo Thanh).

Received October 25, 2025; revised November 19, 2025; accepted December 11, 2025; available online December 15, 2025.

Significant research efforts have been directed toward developing temperature prediction models to support production profile interpretation. Early models rooted in thermodynamic principles have progressively evolved from steady-state to more sophisticated transient and coupled models (Sagar et al., 1991; Hasan et al., 2005, 2009; Wei et al., 2022). These models incorporate factors such as wellbore trajectories, geothermal gradients, and reservoir microthermal processes to improve the physical representation of downhole thermal behavior. Building on this foundation, Alan et al. (2024) proposed a coupled reservoir-wellbore model to predict temperature behavior in single-phase, homogeneous, single-layer reservoirs. Concurrently, researchers focusing on water-flooding development, such as Gan et al. (2024) and Shi et al. (2025), identified key factors that influence reservoir temperature and pressure, although they confined their studies to single-layer scenarios. Notably, Wei et al. (2024) achieved advances by investigating two-phase flow production profile prediction for multilayer commingled gas wells using DTS data, taking an important step toward more realistic production condition modeling. Nevertheless, such physics-based approaches often have high computational costs and limited efficiency when applied to large-scale, high-resolution DTS datasets acquired under actual field operating conditions.

In recent years, machine learning has emerged as a promising approach for interpreting production profiles generated from temperature logs (Matinkia et al., 2023; Jia et al., 2024; Obi et al., 2024; Hui et al., 2025), with significant research efforts initially dedicated to enhancing DTS data quality through noise reduction, resolution improvement, and range expansion monitoring algorithms (Christos et al., 2023; Hayden and Sharma, 2024; Kokhanovskiy et al., 2025). Although these advances substantially improved data acquisition, they simultaneously generated vast volumes of complex temperature data that defied manual interpretation, consequently driving the development of machine-learning-assisted interpretation methods. Artificial neural networks, support vector regression, and random forests have proven successful in identifying flow patterns and estimating phase flow rates under controlled conditions (Shaban and Tavoularis, 2014; Mustafa et al., 2016; Wang et al., 2022; Zhou et al., 2023). However, most existing data-driven approaches remain constrained to single-layer production scenarios and fail to adequately represent the commingled production complexity in multilayer wells. Moreover, operational variability in field environments leads to irregular data that complicate the identification of dominant controlling factors and ultimately limit prediction accuracy.

In view of these limitations, this article introduces a novel method for interpreting wellbore production temperature profiles based on reservoir and wellbore thermodynamics. The proposed model combines conservation laws with seepage dynamics and incorporates key thermal processes to derive characteristic input parameters for sample generation. The researchers employed a combination of back propagation (BP), radial basis function (RBF), and fully connected neural network (FCNN) methods for training and prediction using these datasets. A comprehensive comparison of the three network architectures confirmed a highly effective production profiling approach. Unlike purely data-driven methods, the proposed framework embeds physical constraints into the machine-learning process, ensuring that every input-output pair presented to the neural network remains inherently consistent with underlying physical laws. This design prevents the neural network method from encountering physically implausible data during training, thereby enhancing prediction accuracy and robustness. This research provides a theoretical basis for the interpretation of DTS under single-phase flow conditions and establishes a foundation for extending to more complex scenarios.

2. Method and model

In this study, the researchers selected and compared three neural network algorithms to handle complex DTS data and meet practical field requirements. The BP network algorithm was chosen for its structural simplicity and stable training process, which made it particularly suitable for scenarios involving limited data (Ding et al., 2011). The RBF network algorithm has strong local approximation capabilities, making it ideal for capturing nonlinear temperature distributions (Cervantes et al., 2020). The FCNN network algorithm offers structural flexibility and facilitates the straightforward integration of physical constraints (Azimi et al., 2018). The researchers systematically evaluated these classical but functionally distinct architectures to assess their applicability to physically constrained temperature-output mapping under actual monitoring conditions (Schmidhuber, 2015).

2.1 Neural network method

2.1.1 FCNN

FCNN is classic neural network structures widely used to solve various regression and classification problems. FCNN can effectively extract features from input data and learn potential patterns in data through optimization processes (Kai et al., 2020). For example, they can analyze large-scale multiwell data to capture common trends and differences in production across wells, thereby improving the prediction accuracy of production profiles. This capability provides optimized dynamic forecasting and production scheduling solutions for oil and gas field development.

The fundamental architecture of an FCNN comprises an input layer, several hidden layers, and an output layer. The input layer receives the raw data, with the subsequent layers employing nonlinear activation functions to map the input into a new feature space. Ultimately, the output layer generates the final prediction results.

The core feature of an FCNN is that the neurons in each layer are fully connected to the neurons in the previous layer, allowing the network to handle complex nonlinear relationships. If the input data is denoted as $X = (x_1, x_2, \ldots, x_n)$, where n represents the feature dimension, the output at each layer can be expressed as follows (Goodfellow et al., 2016):

$$h^{(l)} = f\left(W^{(l)} h^{(l-1)} + b^{(l)}\right) \tag{1}$$

where f is the activation function; l is the number of hidden

layers in an FCNN; $l=(1,2,\ldots,n)$; n is the total number of layers in the network; $h^{(l)}$ is the output of the l-th layer; $W^{(l)}$ is the weight matrix of the l-th layer, representing the connection strength of inputs to that layer; and $b^{(l)}$ is the bias term.

Input data pass through the layers to generate the final prediction output. However, the predicted values from the network generally differ from the true values, requiring the use of BP to compute the errors in each layer and update the gradients. Starting from the output layer, the error for each layer is computed as follows (Goodfellow et al., 2016):

$$\delta^{(l)}=\frac{\partial D_F}{\partial \hat{y}_i}f'\left(h^{(l)}\right) \tag{2}$$

where $f'(h^{(l)})$ is the derivative of the activation function with respect to its input, representing the gradient of the activation function in that layer; D_F is the loss function; and $\hat{y}_i$ is the predicted value of the model. For the hidden layers, the error $\delta^{(l)}$ can be recursively calculated using the chain rule (Alpaydin, 2020):

$$\delta^{(l)}=W^{(l+1)}\delta^{(l+1)}f'\left(h^{(l+1)}\right) \tag{3}$$

where $W^{(l+1)}$ is the weight matrix in the $l+1$ layer, $\delta^{(l+1)}$ is the error in the $l+1$ layer, and $f'(h^{(l+1)})$ is the derivative of the activation function in the $l+1$ layer.

Once the errors have been computed, the weights are updated using gradient descent. Assuming the learning rate is η, the weight update formula W is as follows (Alpaydin, 2020):

$$W^{(l+1)}=W^{(l)}-\eta\frac{\partial D_F}{\partial W^{(l)}} \tag{4}$$

where the gradient formula is:

$$\frac{\partial D_F}{\partial W^{(l)}}=\delta^{(l)}h^{(l-1)} \tag{5}$$

Since the aim of this study was to enhance multilayer production profile prediction and better capture the probabilistic characteristics of the output, the researchers used a Gaussian likelihood function as the loss function for training (Zhang et al., 2018):

$$D_F=-\sum_{i=1}^{N}\log\left\{\frac{1}{\sqrt{2\pi\sigma^2}}\exp\left[-\frac{(\hat{y}_i-y_i)^2}{2\sigma^2}\right]\right\} \tag{6}$$

where y_i is the actual value, and σ^2 is the variance of the prediction error.

Using the Gaussian likelihood function as the loss function for BP resulted in the optimization of the network to achieve optimal parameter values. The training and prediction process for the network model is illustrated in Fig. 1, and the flowchart of the FCNN model is shown in Fig. 2.

2.1.2 RBF neural network method

RBF neural networks are feed-forward architectures characterized by three-layer structures and localized approximation properties (Ma et al., 2024). The input layer interfaces with external data through the source nodes, while a single hidden layer performs nonlinear transformations. A linear output layer subsequently generates predictions based on activations propagated from hidden units (Kumar et al., 2025). The training process relies on a dual optimization strategy: Linear weights between the hidden and output layers are updated through efficient linear optimization, while hidden-layer parameters governing activation functions undergo nonlinear adjustment. Hidden units construct a set of basic functions that span the transformed feature space when input vectors are projected into the hidden layer. These functions, typically implemented as Gaussian functions, provide the foundational mechanism for the network's approximation capability.

2.1.3 BP neural network method

BP networks are neural networks that calculate output values and then work backward through the networks to compute the corresponding input values (Wang et al., 2016). Errors are calculated by comparing the back-calculated input values with the original inputs. If an error exceeds a specified threshold, the connection weights are adjusted and recalculated until the error meets the desired criteria. This method is particularly valuable because it addresses the difficulty of determining hidden layer parameters. The BP neural network is a multilayer feedforward neural network.

2.1.4 Effect evaluation index

Following the BP process, the errors between the network outputs and the actual targets had to be calculated. The error values could then be used to evaluate the model's performance. In this study, the mean absolute error (MAE), root mean squared error (RMSE), and coefficient of determination (R^2) were computed for the BP neural network, RBF neural network, and FCNN to compare the optimization results and prediction accuracy of the three models (Milan et al., 2015), as follows:

$$\mathrm{MAE}=\frac{1}{m}\sum_{i=1}^{m}|y_i-\hat{y}_i| \tag{7}$$

$$\mathrm{RMSE}=\sqrt{\frac{1}{m}\sum_{i=1}^{m}(y_i-\hat{y}_i)^2} \tag{8}$$

$$\mathrm{R}^2=1-\frac{\sum_i(\hat{y}_i-y_i)^2}{\sum_i(\bar{y}_i-y_i)^2} \tag{9}$$

where m is the number of samples, and $\bar{y}_i$ is the mean value.

2.2 Production layer temperature model

Next, the researchers simplified the oil flow conditions by focusing on single-phase flow to establish a clear mechanistic thermodynamic model for wellbore heat transfer and to validate its reliability. In this model, strong nonlinear coupling effects introduced by phase change, gas-liquid slip, and complex flow patterns were not considered, which allowed the researchers to concentrate on elucidating the fundamental mechanisms of heat conduction and convective heat transfer between the wellbore and the formation.

Based on this, a wellbore temperature distribution prediction model was developed to determine the temperature profile along the wellbore. The forward model was based on the principles of mass and energy conservation. Fig. 3 shows the

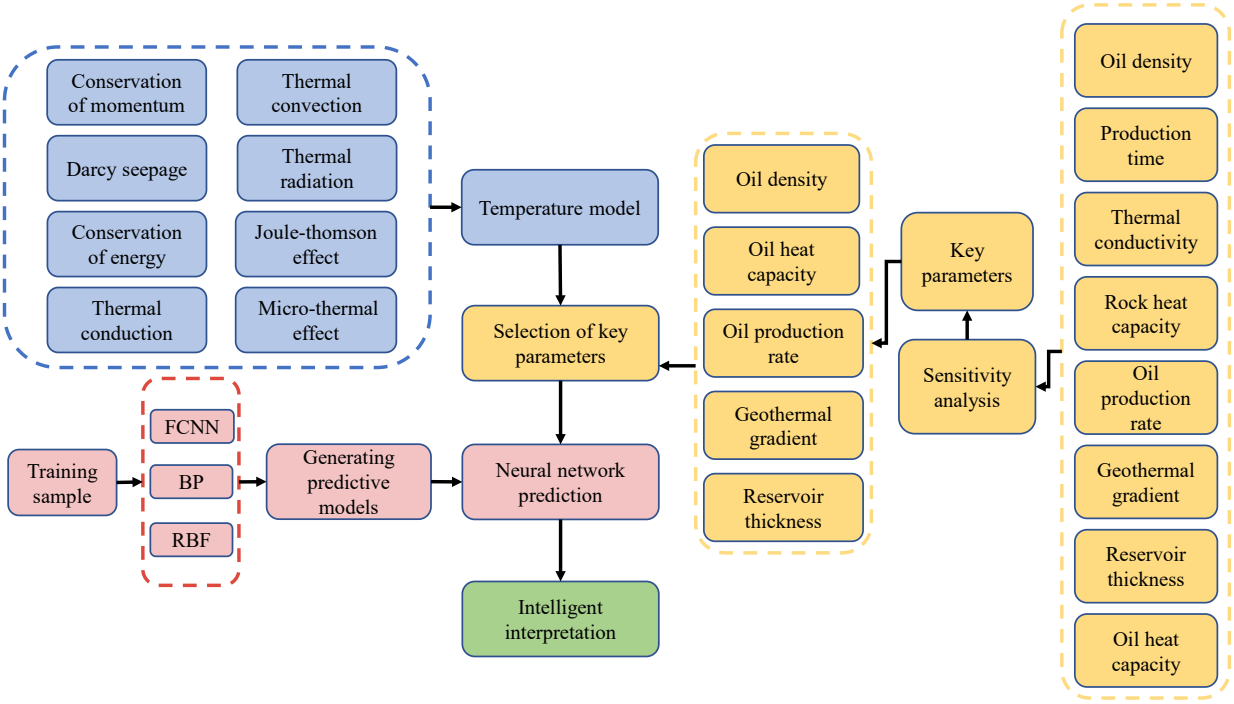

Fig. 1. FCNN training and prediction processes.

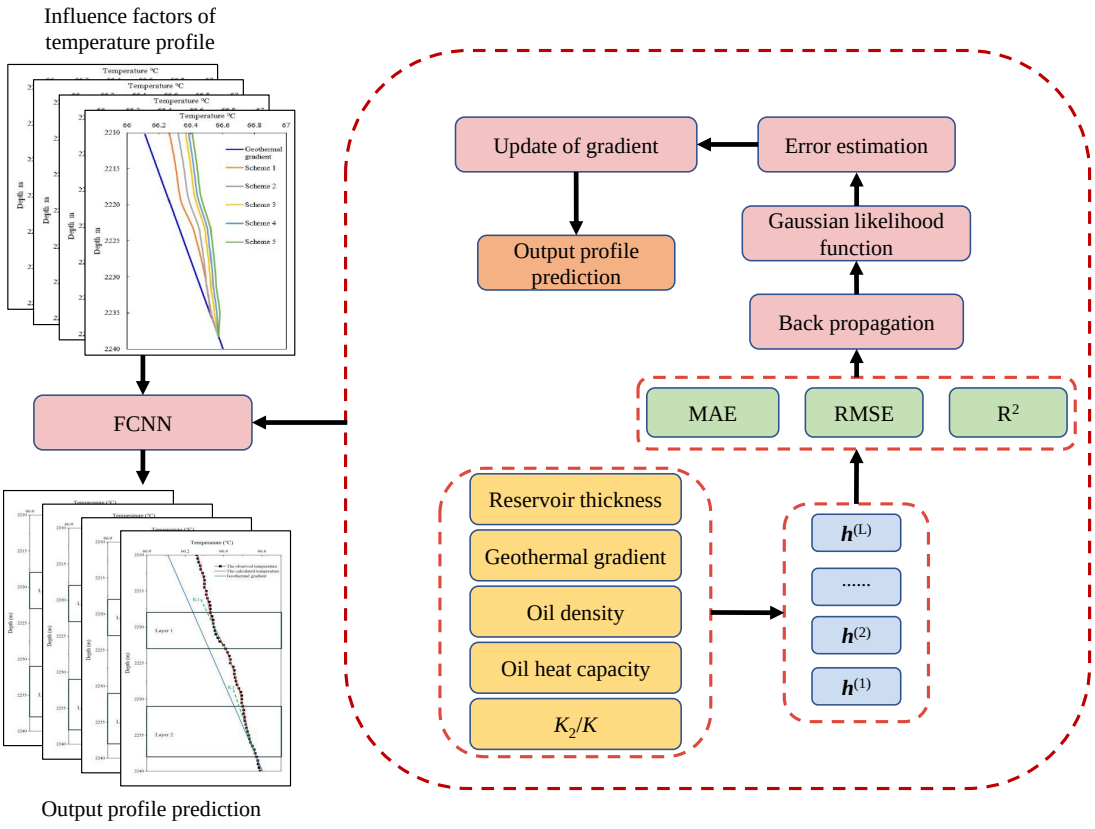

Fig. 2. Production profile prediction flowchart based on the FCNN algorithm.

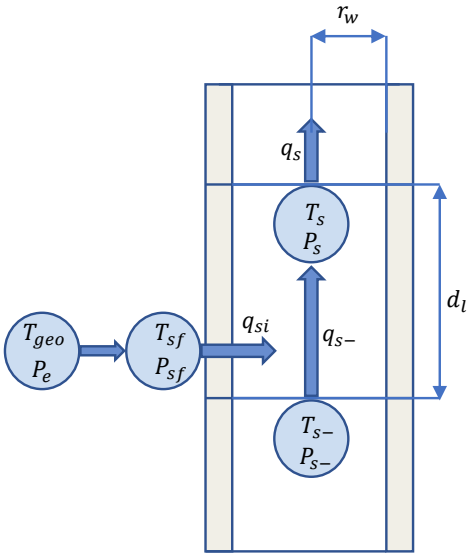

Fig. 3. Production well diagram.

dynamic movement of the fluid. The flow process comprises two distinct stages: 1) The flow of formation fluid toward the wellbore and 2) the flow of fluid upwards within the wellbore.

Using a well segment as an example, the researchers considered a small region within the wellbore with a length of dl, located at the front of a reservoir block. The energy accumulation equation is as follows:

$$\frac{\mathrm{d}E}{\mathrm{d}t} = E_{\text{in}} - E_{\text{out}} \tag{10}$$

where E is the total energy in the wellbore, E_{in} is the energy entering the segment, E_{out} is the energy exiting the segment, and t is the time.

The energy concentration per unit of mass is as follows:

$$e = u + \frac{1}{2}v^2 + gdl \tag{11}$$

where e is the specific energy, u is the internal energy, v is the kinetic energy term, g is the gravitational acceleration, and dl is a small region within the wellbore with a length of dl.

For a producing well, the energy flowing into the segment (E_{in}) can be further subdivided into three segments: The energy carried by the fluid entering the downhole pipeline (q_{s-}), the energy carried by the formation fluid (q_{is}), and the thermal energy transmitted from the reservoir. By combining the concept of energy concentration with expansion work, the energy balance can be further expanded as follows:

$$\begin{aligned}\frac{\mathrm{d}E}{\mathrm{d}t} = {} & q_{s-}\rho_{s-}e_{s-} + q_{is}\rho_{is}e_{is} - q_s\rho_s e_s \\ & + D\Delta T + q_{s-}P_{s-} - q_s P_s\end{aligned} \tag{12}$$

where q_{s-} is the mass flow rate in the lower part of the discrete segment, ρ_{s-} is the fluid density in the lower part of the discrete segment, e_{s-} is the specific energy in the lower part of the discrete segment, q_{is} is the mass flow rate in the middle part of the discrete segment, ρ_{is} is the fluid density in the middle part of the discrete segment, e_{is} is the specific energy in the middle part of the discrete segment, q_s is the mass flow rate in the upper part of the discrete segment, ρ_s is the fluid density in the upper part of the discrete segment, e_s is the specific energy in the upper part of the discrete segment, D is the coefficient of heat conduction, T is the temperature, P_{s-} is the pressure in the lower part of the discrete segment, and P_s is the pressure in the upper part of the discrete segment.

The definition of enthalpy is as follows:

$$h = u + \frac{P}{\rho} \tag{13}$$

where h is the thermal enthalpy, P is the pressure, and ρ is the fluid density.

Combined with the above, the energy balance for a certain segment of the wellbore can be expressed as follows:

$$\frac{\mathrm{d}E}{\mathrm{d}t} = q_{s-}\rho_{s-}\left[h_{s-} + \frac{1}{2}\left(\frac{q_{s-}}{A\rho_{s-}}\right)^2 + gdl\right] + q_{is}\rho_{is}\left[h_{sf} + \frac{1}{2}\left(\frac{q_{sf}}{A\rho_{sf}}\right)^2 + gdl\right] - q_s\rho_s\left[h_s + \frac{1}{2}\left(\frac{q_s}{A\rho_s}\right)^2\right] + D\Delta T \tag{14}$$

where h_{s-} is the thermal enthalpy in the lower part of the discrete segment, A is the wellbore area, h_{sf} is the thermal enthalpy of sand, q_{sf} is the mass flow rate of sand, ρ_{sf} is the fluid density of sand, and h_s is the thermal enthalpy of discrete segments of sand.

According to the general energy balance equation, under steady-state flow conditions, the vertical thermal conductivity coefficient could be eliminated to obtain the energy balance equations for the wellbore and reservoir under different conditions, as follows:

Wellbore energy balance equation E_1:

$$E_1 = q_{s-}\rho_{s-}\left[h_{s-} + \frac{1}{2}\left(\frac{q_{s-}}{A\rho_{s-}}\right)^2 + gdl\right] + q_{is}\rho_{is}\left[h_{sf} + \frac{1}{2}\left(\frac{q_{is}}{A\rho_{sf}}\right)^2 + g\frac{dl}{2}\right] - q_s\rho_s\left[h_s + \frac{1}{2}\left(\frac{q_s}{A\rho_s}\right)^2\right] + D_{wb}\left(T_{sf} - \bar{T}_s\right) = 0 \tag{15}$$

where D_{wb} is the wellbore thermal conductivity, T_{sf} is the temperature of the sand surface, and $\bar{T}_s$ is the average temperature of the sand surface.

Reservoir energy balance equation E_2:

$$\begin{aligned}E_2 = {} & q_{is}\rho_{is}\left[h_{sf} + \frac{1}{2}\left(\frac{q_{sf}}{A\rho_{sf}}\right)^2 - h_{res}\right] \\ & + D_{wb}\left(T_{sf} - \bar{T}_s\right) + D_{res}\left(T_{sf} - T_{geo}\right) = 0\end{aligned} \tag{16}$$

Table 1. Production interval of well X.

Layer	Production interval (m)	Permeability (mD)
1	2,219-2,224	430
2	2,232-2,239	160

where D_{res} is the reservoir thermal conductivity, T_{geo} is the formation temperature, and h_{res} is the reservoir thermal enthalpy.

For each well unit, the energy balance (E_1) includes convective heat flux (the internal, kinetic, and potential energy transferred by the fluid movement from the lower section to the upper section and the reservoir), as well as the convective heat flux between the wellbore surface and the unit itself. The energy balance (E_2) for each well unit includes convective heat flux (the internal, kinetic, and potential energy transferred by the fluid movement from the lower section to the upper section and the reservoir), as well as the convective heat flux between the wellbore surface and the unit, and between the wellbore surface and the reservoir.

Heat loss coefficient:

$$D_{res} = \frac{2\pi\lambda^*_{res} dL}{\ln\frac{r_e}{r_w}} \tag{17}$$

$$D_{wb} = 2\pi U dL r_w \tag{18}$$

where λ^*_{res} is the characteristic viscosity loss coefficient, U is the overall heat transfer coefficient of the wellbore, dL is the length of the oil pipe, r_e is the outer radius, and r_w is the inner radius.

The expression of U in Eq. (18) is as follows:

$$\frac{1}{U} = \frac{r_{to}}{k_t}\ln\frac{r_{to}}{r_{ti}} + \frac{r_{to}}{k_{ann}}\ln\frac{r_{ci}}{r_{to}} + \frac{r_{to}}{k_c}\ln\frac{r_{co}}{r_{ci}} + \frac{r_{to}}{k_{cem}}\ln\frac{r_w}{r_{co}} + \frac{r_{to}}{r_{ci}(h_c+h_v)} \tag{19}$$

where r_{to} is the outer diameter of the oil pipe, r_{ti} is the inner diameter of the oil pipe, r_{co} is the outer diameter of the casing, r_{ci} is the inner diameter of the casing, k_t is the thermal conductivity of the oil pipe, k_{ann} is the annular layer thermal conductivity, k_c is the thermal conductivity of the casing, k_{cem} is the thermal conductivity of the drilling mud, h_c is the natural convection heat transfer coefficient, and h_r is the thermal radiation.

Substituting Eq. (19) into Eq. (18), D_{wb} can be written as follows:

$$D_{wb} = dL\left(\frac{1}{2\pi k_t}\ln\frac{r_{to}}{r_{ti}} + \frac{1}{2\pi k_{ann}}\ln\frac{r_{ci}}{r_{to}} + \frac{1}{2\pi k_c}\ln\frac{r_{co}}{r_{ci}} + \frac{1}{2\pi k_{cem}}\ln\frac{r_w}{r_{co}}\right)^{-1} = \frac{D^{(1)}_{wb}D^{(2)}_{wb}}{D^{(1)}_{wb}+D^{(2)}_{wb}} \tag{20}$$

$$D^{(1)}_{wb} = dL\left(\frac{1}{2\pi k_t}\ln\frac{r_{to}}{r_{ti}} + \frac{1}{2\pi k_{ann}}\ln\frac{r_{ci}}{r_{to}}\right)^{-1} \tag{21}$$

$$D^{(2)}_{wb} = dL\left(\frac{1}{2\pi k_c}\ln\frac{r_{co}}{r_{ci}} + \frac{1}{2\pi k_{cem}}\ln\frac{r_w}{r_{co}}\right)^{-1} \tag{22}$$

where $D^{(1)}_{wb}$ is the thermal conductivity of the oil pipe and annular layer, and $D^{(2)}_{wb}$ is the thermal conductivity of the casing and drilling mud.

Since there were two nodes in the reservoir, an additional equation ΔP_{sf-e} was required to relate P_e to P_{sf}. This equation is the steady-state Darcy equation, which also considers the effect of the skin factor:

$$\Delta P_{sf-e} = P_e - P_{sf} = \frac{Q\mu}{2\pi k_H h_T}\left(\frac{h_T}{L_w}S + \ln\frac{r_e}{r_w} + S_G\right) \tag{23}$$

where P_e is the formation static pressure, P_{sf} is the sand face inflow pressure, Q is the volumetric flow rate, μ is the fluid viscosity, k_H is the formation permeability, h_T is the reservoir thickness, L_w is the wellbore length, S_G is the geometric skin, and S is the mechanical skin factor.

Positive skin factor:

$$P_{sf} = P_s + \frac{Q\mu S}{2\pi k_H L_w} \tag{24}$$

$$P_e = P_{sf} + \frac{Q\mu}{2\pi k_H h_T}\left(\ln\frac{r_e}{r_w} + S_G\right) \tag{25}$$

Negative skin factor:

$$P_{sf} = P_s \tag{26}$$

$$P_e = P_{sf} + \frac{Q\mu}{2\pi k_H h_T}\left(\ln\frac{r_e}{r_w} + S_G + \frac{h_T}{L_w}S\right) \tag{27}$$

After determining an average pressure point in a wellbore segment and the flow temperature in the wellbore, iterative calculations could be performed to determine P_e and P_{sf} at different locations. Combining the earlier energy equations allowed the researchers to obtain the temperature profiles of the wellbore fluid T_s and the formation fluid T_{sf}.

Based on the established wellbore temperature forward model and neural network methods, the technical roadmap for this study is shown in Fig. 4.

3. Optimization of temperature parameters and neural network models

3.1 Temperature-influencing parameters

Based on the theoretical model and calculation process explained in the previous section, production profile temperature interpretation was conducted. The impact of different sensitivity parameters on the production temperature was analyzed using forward simulations, considering the impact of factors such as oil production, geothermal gradient, and crude oil density on the temperature response slope. As illustrated in Table 1, the data were organized according to a specific production segment of well X. The results presented in Table 2 and Fig. 5 demonstrate the variations in the slope for different production rates from production layer 2. In these figures, K represents the geothermal gradient slope, K_3 is the temperature slope for the lower wellbore, K_2 is the temperature slope for the upper 4-8 m of the lower section, and K_1 is the temperature slope for the upper wellbore. These four parameters were used to collectively and accurately characterize the trend of temperature variations.

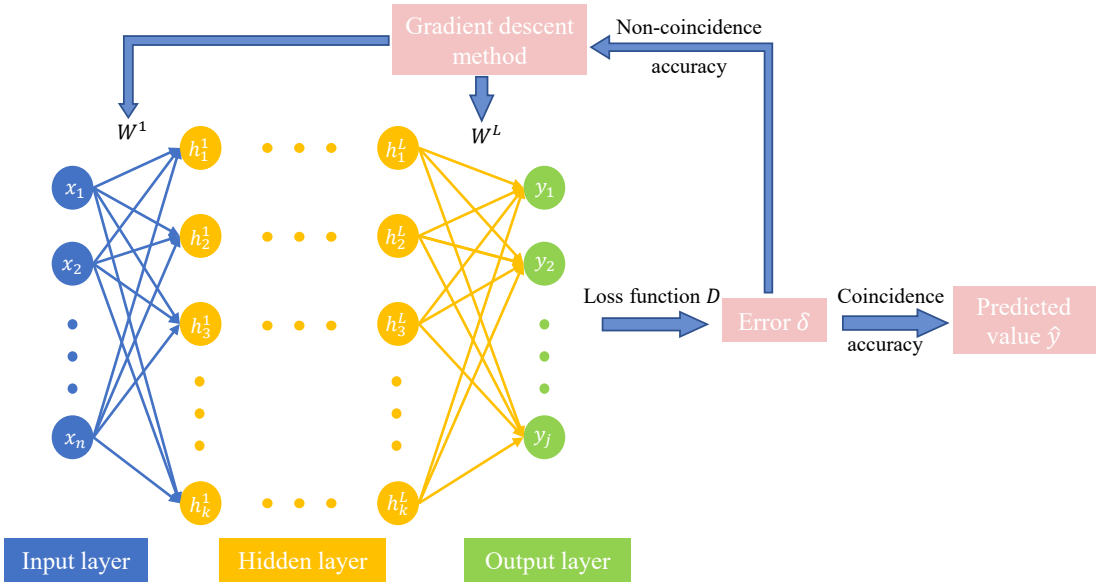

Fig. 4. Intelligent predictive technology roadmap.

Table 2. Basic parameters for different production rates from production layers 1 and 2.

Layer	Scheme	Oil rate (m^3/d)	K_1 (m/°C)	K_2 (m/°C)	K_3 (m/°C)	K_1/K	K_2/K	K_3/K
1	1	1.38	126.970	53.682	125.750	2.095	0.886	2.075
	2	2.38	137.100	128.290	145.090	2.262	2.117	2.394
	3	3.38	139.070	70.396	158.860	2.295	1.162	2.621
	4	4.38	144.790	170.170	268.770	2.389	2.808	4.335
	5	5.38	149.710	179.330	166.740	2.470	2.959	4.751
2	1	2.4	53.682	89.745	93.268	0.886	1.481	1.539
	2	4.4	55.746	89.744	93.268	0.92	1.481	1.539
	3	6.4	60.008	89.744	93.268	0.99	1.481	1.539
	4	8.4	76.331	89.744	93.268	1.259	1.481	1.539
	5	10.4	113.33	89.744	93.268	1.87	1.481	1.539

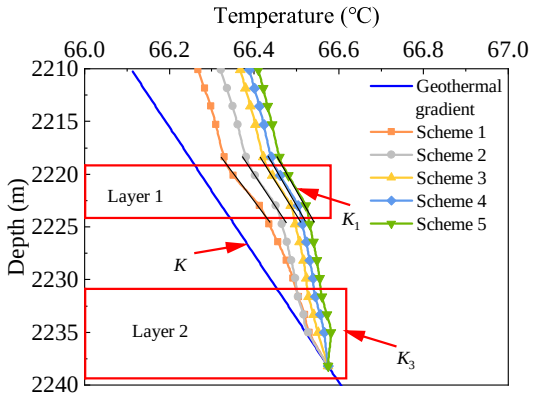

Fig. 5. Temperature response curves for different volumes of oil production from production layer 2.

To evaluate the impact of production rates on temperature distribution, a sensitivity analysis was conducted. As shown in Table 2 and Fig. 5, the wellbore temperature exhibited a clear increasing trend with rising oil production, indicating a significant influence of production volume on thermal behavior. Furthermore, as the production from layer 2 ($K = 60.606$ m/°C) increased proportionally, the temperature slopes for layer 1, layer 2, and the intermediate section, represented by K_1, K_2, and K_3, all increased accordingly. The normalized slope ratios K_1/K, K_2/K, and K_3/K also showed consistent growth, reflecting an enhanced thermal response under higher production conditions.

To assess the influence of production variations in the upper reservoir, the temperature response of production layer 1 ($K = 60.606$ m/°C) was systematically analyzed. As summarized in Table 2 and Fig. 6, a clear positive correlation was observed between oil production and wellbore temperature, with production volume exerting a pronounced thermal effect. As the production rate from layer 1 increased proportionally,

Table 3. Basic parameters for different geothermal gradients.

Layer	Oil production (m^3/d)	Formation temperature (°C)
1	8.4	66.595
2	1.38	66.628

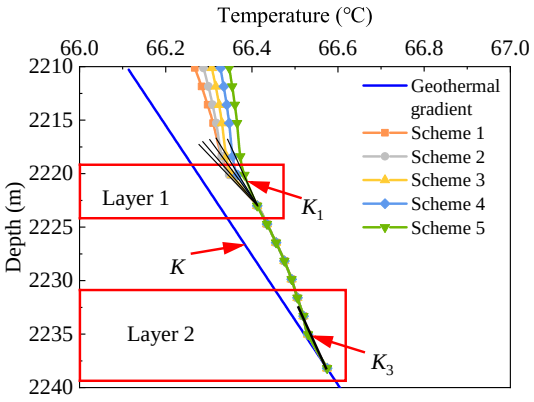

Fig. 6. Temperature response curves for different volumes of oil production from production layer 1.

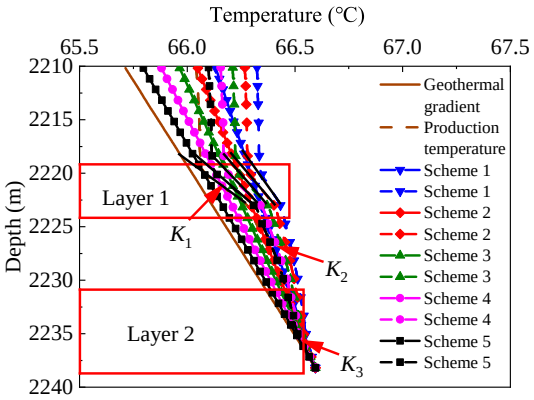

Fig. 7. Temperature response curves for different production layers with varying geothermal gradients.

both the absolute temperature slope K_1 and the normalized slope ratio K_1/K exhibited a gradual rise. In contrast, the production rate in the upper layer showed a negligible impact on the temperature gradient in the lower wellbore sections.

To further investigate thermal behavior under varying geothermal conditions, additional simulations were performed for both production layers. Table 3 summarizes the simulated wellbore temperature profiles for different formation temperature gradients, and the resulting slope variations according to these gradients are presented in Table 4 and Fig. 7. The simulation results indicated that an increasing geothermal gradient led to a decrease in the wellbore temperature. Specifically, the normalized slope ratio K_1/K gradually declined, whereas K_2/K and K_3/K exhibited corresponding increases.

Additionally, the influence of reservoir thickness, production time, rock thermal conductivity, crude oil thermal conductivity, crude oil heat capacity, and crude oil density on the production temperature profile was simulated, and the results are shown in Figs. S1-S6 (in the Supplementary file). From the figures, it is evident that production time and crude oil thermal conductivity had negligible impacts on the production temperature profile. Conversely, an increase in reservoir thickness and rock thermal conductivity resulted in a decrease in wellbore temperature. The heat capacity of crude oil exerted a substantial influence on the temperature, as evidenced by the observation that as the heat capacity increased, the ratio of K_1 to the K_1/K temperature slopes also increased. However, this effect had no substantial impact on the lower section temperature slopes. The influence of crude oil density on temperature was obvious. It is known that the magnitude of crude oil density directly correlates with the ratio of K_1 to the K_1/K temperature slope, with a concomitant decrease in the degree of influence. However, as the depth increases, the influence on the temperature slope of the lower interval decreases.

Preliminary findings from the forward simulation analysis indicated that the primary factors influencing production temperature were oil production, geothermal gradient, reservoir thickness, crude oil heat capacity, and crude oil density. To further quantify their relative impacts, a local normalized sensitivity coefficient S_c was introduced, defined as:

$$S_c = \frac{|\Delta Y/Y_{ref}|}{|\Delta X/X_{ref}|} \tag{28}$$

where ΔY is the change in the temperature slope, Y_{ref} is the reference value of the temperature slope, ΔX is the change in the input parameter, and X_{ref} is the reference value of the input parameter.

As illustrated in Table 5, the impact of the previously identified main controlling factors was quantitatively substantiated. Among these factors, oil production was identified as the primary contributor to temperature fluctuations. Conversely, production time and rock thermal conductivity exhibited minimal influence on the production temperature profile and could be disregarded.

3.2 Neural network models

By analyzing the response characteristics of the pure oil production temperature profile, it was determined that the meanings represented by the three parameters K_1, K_2, and K_3 were analogous but represented different positions. However, K_2 indicated the temperature response of the intermediate transition layer section. This layer section was subject to the effects of both heat loss from the upper layer and heat contribution from the lower layer. Concurrently, these phenomena reflected the production influences of both the upper and lower layers. Furthermore, compared with K_1 and K_3, K_2 was a nonperforated section that was less influenced by additional factors during the development process, with more stable changes, which more accurately reflected the influence of reservoir physical properties. Therefore, to simplify the model, only K_2 was used in the subsequent analysis. Following a thorough analysis of the available data, five parameters were ultimately selected for use in the intelligent interpretation mo-

Table 4. Basic parameters for multiple schemes at different geothermal gradients.

Scheme	dT/dZ (°C/100 m)	K (m/°C)	K_1 (m/°C)	K_2 (m/°C)	K_3 (m/°C)	K_1/K	K_2/K	K_3/K
1	1.65	60.606	41.790	89.748	93.262	0.690	1.481	1.539
2	1.95	51.282	33.685	76.255	76.850	0.657	1.487	1.499
3	2.25	44.444	28.213	66.289	65.350	0.635	1.492	1.470
4	2.55	39.216	24.270	58.626	56.843	0.619	1.495	1.449
5	2.85	35.088	21.294	52.552	50.296	0.607	1.498	1.433
6	3.15	31.746	18.968	47.617	45.101	0.597	1.500	1.421

Table 5. Sensitivity analysis of different factors.

Factors	S_c
Oil production	0.136
Geothermal gradient	0.086
Reservoir thickness	0.057
Crude oil heat capacity	0.053
Crude oil density	0.026
Production time	0.0031
Rock thermal conductivity	0.0029

del: Reservoir thickness, crude oil density, crude oil heat capacity, geothermal gradient, and K_2/K. A simulation was conducted to predict the production temperature profiles for 5,000 combinations of these parameters, resulting in prediction samples for single-phase oil well production profiles. The simulation results are shown in Table 6, with only a selection of the combinations presented due to the large number of scenarios.

Based on the sample data shown in Table 6, BP neural network, RBF neural network, and FCNN were trained and tested for prediction. To mitigate overfitting and enhance model generalizability, L2 regularization with a coefficient of 0.0001 was consistently applied as a unified strategy across all three neural network architectures during the training process. The relationship between oil production rate and temperature, as explained in Section 3.1, was used to invert predicted temperatures and estimate production rates. The most effective automated production rate interpretation method was determined through comparative analysis.

(1) Training for BP parameters

Based on the 5,000 sample datasets, 3,500 samples were randomly selected for training, and the remaining 1,500 samples were used for prediction. The BP neural network prediction method was applied, and the impact of three parameters-prediction set proportions, number of neurons, and iteration counts-on the prediction results was optimized. Figs. S7(a)-S7(c) in the Supplementary file show comparisons between the predicted and actual production rates under different prediction set proportions, neuron numbers, and iteration counts.

Table 6. Combined schemes (partial display).

Reservoir thickness (m)	Oil density (kg/m^3)	K_2/K	Oil heat capacity (J/(kg·°C))	dT/dZ (°C/100 m)	Oil production (m^3/d)
5.6	870	1.683395	1,800	2.17	18
6.6	885	1.02708	1,800	1.77	2
6.6	870	1.938463	2,050	1.97	16
6.6	870	1.030671	1,800	1.97	2
5.6	885	1.229454	1,800	1.77	12
4.6	895	1.021985	1,900	1.77	16
6.6	870	1.464179	1,900	1.97	8
5.6	895	1.109277	1,800	1.77	18
5.6	870	1.915658	2,050	2.17	18
4.6	870	1.298036	1,800	1.97	10
5.6	885	1.141264	1,800	1.77	6
4.6	895	1.024705	1,900	1.77	12
4.6	870	1.206136	1,900	1.77	6
5.6	885	1.168967	2,050	1.77	4
5.6	885	1.325401	1,900	1.77	14
5.6	870	1.716468	1,800	2.17	20
5.6	895	1.13619	1,900	1.77	8
5.6	885	1.112407	1,900	1.77	4
6.6	870	1.470611	1,800	2.17	8
4.6	870	1.427945	2,050	1.77	12
4.6	885	1.033844	1,800	1.77	4
4.6	870	1.479699	1,800	2.17	18
5.6	870	1.800281	1,900	2.17	18

(2) Training for RBF parameters

Similarly, 3,500 samples were randomly selected for training, and the remaining 1,500 samples were used for prediction. The RBF neural network prediction method was applied, and the impact of three parameters (RBF density, learning rates, and prediction set proportions) on the prediction results was optimized. Figs. S8(a)-S8(c) in the Supplementary file show

Table 7. Best parameters for the three neural network models.

Method	Parameter	Value
BP	Prediction sets	0.2
	Neurons	3
	Iteration counts	400
RBR	Prediction sets	0.2
	Density	400
	Learning rates	0.001
FCNN	Optimizers	Nadam
	Prediction sets	0.2
	Neurons	128
	Batch sizes	4

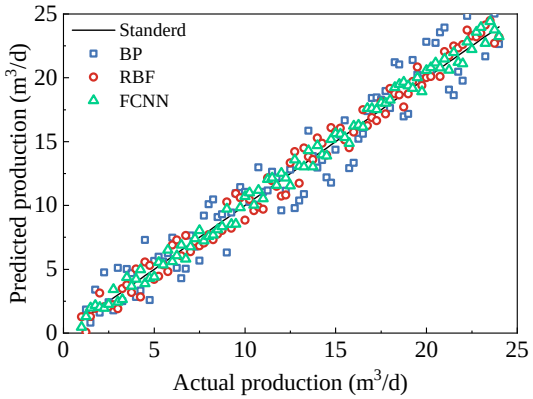

Fig. 8. Comparison of the three prediction methods with actual production rates.

comparisons between the predicted and actual production rates under different predictions of the proportion of sets, radial basis densities, and learning rates.

(3) Training for FCNN parameters

Again, 3,500 samples were randomly selected for training, and the remaining 1,500 samples were used for prediction, as in the previous method. The FCNN method was used for prediction, and the model demonstrated both high generalization ability and prediction accuracy. Based on a feasibility analysis of the FCNN prediction method, the optimization of four parameters (optimizers, prediction set proportions, neuron numbers, and batch sizes) was conducted using the sample data. Figs. S9(a)-S9(d) in the Supplementary file show comparisons between the predicted and actual production rates under different optimizers, prediction set proportions, neuron numbers, and batch sizes.

Based on the parameter sensitivity analysis, the optimal parameters for each neural network model were determined (see Table 7). Comparative analyses of the three models (BP, RBF, and FCNN) are presented in Fig. 8 and Table 8, demonstrating that the FCNN model achieved superior overall performance, with the highest coefficient of determination (R^2) and the most consistent prediction accuracy. To further validate these findings and mitigate potential bias from individual metrics, a global performance index (GPI) was employed (Milan et al., 2015).

Table 8. Comparison of accuracy parameters for the prediction results based on the three methods.

Method	MAE	RMSE	R^2	GPI
FCNN	0.3389	0.2347	0.9106	1.081
RBF	0.4425	0.2309	0.8586	0.016
BP	0.5102	0.4615	0.8011	-1.904

$$\mathrm{GPI} = \sum_{j=1}^{3} \alpha_j \left(\tilde{y}_j - y_{\theta j}\right) \tag{29}$$

where $\tilde{y}_j$ is the median of the scaled values of indicator j, y_{ij} is the scaled value of indicator j for model i, and α_j equals 1 for $j = 3$ (R^2) and -1 for all other indicators.

The GPI integrates multiple evaluation criteria into a single composite score, which provided a more robust basis for model comparison in this study, as shown in Table 8. According to the GPI analysis, the models were ranked as follows: FCNN, RBF, and BP. This quantitatively confirmed that the FCNN model outperformed the other two models. The BP model demonstrated the poorest performance, with the lowest prediction accuracy, whereas the RBF model exhibited moderate prediction performance. All three models demonstrated the capacity to predict production capacity; however, the FCNN model yielded predictions that were more precise and reliable. Notably, all models maintained low computational costs during training. This efficiency stemmed from the use of a physics-based forward model to generate training data and a carefully selected, low-dimensional set of input parameters, which collectively and significantly reduced the computational burden.

4. Field application

4.1 Preprocessing of field DTS data: Noise and outlier handling

The forward model and neural network training described in the previous sections were based on steady-state simulation data, which validated the core feasibility of the method in a controlled, noise-free environment. However, the researchers recognized that DTS data acquired in the field are inherently dynamic and inevitably contaminated by noise. Directly feeding raw, noisy data into the trained model would have severely compromised the accuracy and reliability of the prediction results.

To enhance the generalization capability and robustness of the intelligent interpretation method when applied to field data, a dedicated data preprocessing workflow was introduced prior to inputting the field data into the FCNN model. Preprocessing consists of two sequential steps:

1) Outlier detection and removal using the Z-score (Ma

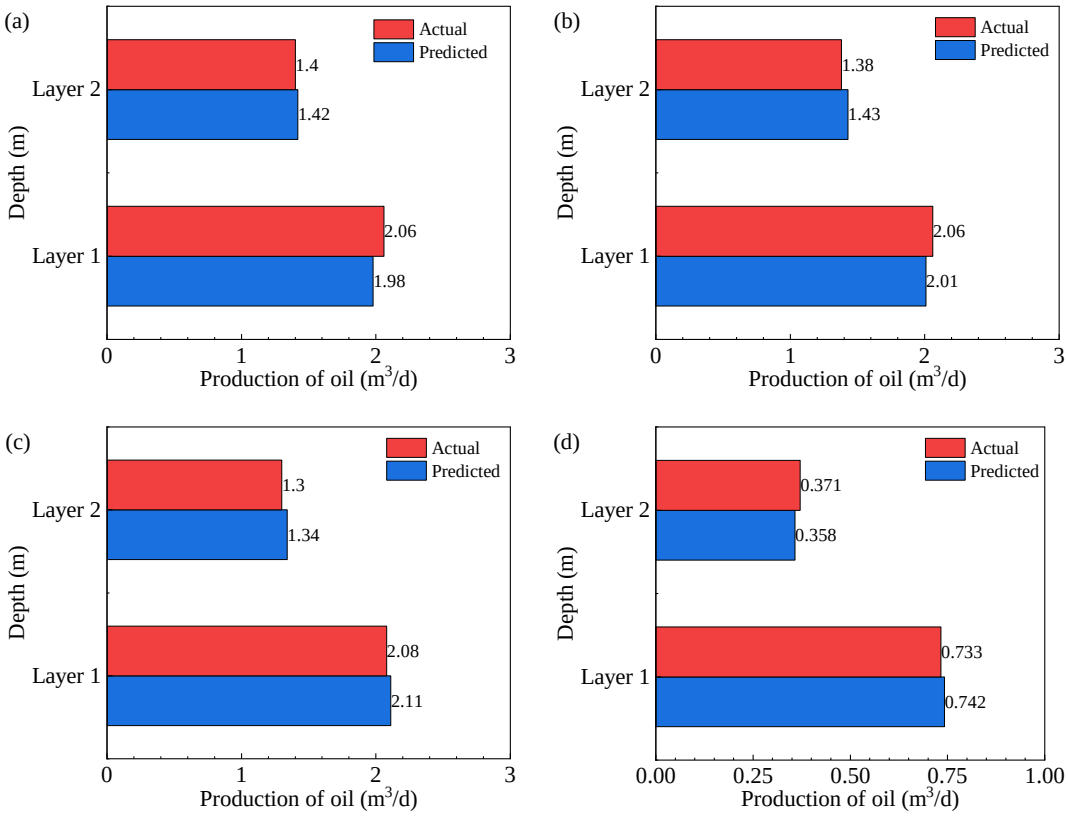

Fig. 9. Comparisons of predicted and actual production rates: (a) Well XX-77-1 4/10, (b) Well XX-77-1 4/12, (c) Well XX-77-1 4/18 and (d) Well XX-18-1 5/08.

and Zhu, 2013): The first step aims to identify and remove significant outliers that deviate drastically from the overall temperature profile. The Z-score – a measure of how many standard deviations a data point is from the mean – was employed for this purpose. The Z-score was calculated as follows for a temperature value T_i at depth i, as follows:

$$z = \frac{T_i - \mu}{\sigma} \tag{30}$$

where z is the Z-score standardized output data, and μ and σ are the average and standard deviations of the data set. Any data point with a Z-score that exceeded a threshold of 3 was considered an outlier and was removed. The removed values were then interpolated using a linear method based on neighboring valid data points.

2) For noise suppression in the processed temperature profiles, a Savitzky-Golay filter was applied following outlier removal (Savitzky and Golay, 1985). This approach effectively attenuated high-frequency fluctuations while maintaining the fidelity of key thermal transition features. In contrast to conventional moving average techniques, which may distort signal morphology, the Savitzky-Golay algorithm operates by performing local polynomial regression on successive data segments through linear least-squares fitting. This ensures effective noise reduction without substantially compromising the resolution of salient temperature variations. Through empirical evaluation, a configuration employing an 11-point window and a second-order polynomial was adopted.

4.2 Application to well

Based on the preprocessing algorithm and the physically constrained intelligent interpretation method established in this study, the model was validated using actual DTS monitoring data from two producing wells in the Qingyuan structural zone within the Baoding depression, and the target formation exhibited a geothermal gradient of 2.20 °C/100 m. Both Well XX-77-1 and Well XX-18-1 were equipped with permanent distributed fiber-optic monitoring systems installed outside the casing, located in the 77X and 18X blocks, respectively. The key production layer parameters for both wells, along with the corresponding temperature monitoring data used for interpretation, are summarized in Table 9.

The intelligent interpretation algorithm developed in this study was applied to analyze production performance. As shown in Figs. S10(a)-S10(d) (in the Supplementary file), the computed temperature matched the observed data very well, with minimal error, and the temperature distribution was primarily controlled by the K_2/K ratio. Based on the baseline parameters for intelligent interpretation shown in Table 9, automated interpretation of production profiles for two wells was conducted using commercial software. The results presented in Fig. 9 show strong correlations between the predicted results and the actual production rates, with the absolute error for each layer being less than 3.88%, demonstr-

Table 9. Production segment parameters for Wells XX-77-1 and XX-18-1.

Well	Date	Thickness (m)	Oil density (kg/m^3)	K_2/K
77-1	4/10	6.6	0.89	1.015
	4/12	6.6	0.89	1.018
	4/18	6.6	0.89	1.014
18-1	5/08	6.0	0.87	1.325

ating the effectiveness of the method. The intelligent interpretation algorithm established in this study therefore provides a foundation for field-scale reservoir management and well-level production decision-making by facilitating the effective interpretation of reservoir production behavior.

5. Conclusions

1) In this article, the researchers propose a forward model for production well temperature profiles in wellbores based on the principles of momentum conservation, energy conservation, and two-phase flow theory. The model revealed the influence of various factors-oil production, geothermal gradient, reservoir thickness, crude oil heat capacity, crude oil density, production time, and rock thermal conductivity-on production temperature. It identified oil production, geothermal gradient, reservoir thickness, crude oil heat capacity, and crude oil density as the primary controlling factors. The model incorporates an FCNN, an RBF neural network, and a BP neural network for training and prediction, which the researchers used for intelligent interpretation method optimization.
2) The creation of 5,000 combination schemes as single-phase oil well production profile prediction samples was based on the aforementioned controlling factors. Three neural network methods were used for training and prediction based on the sample data, and a comparative analysis of the three methods was performed. The findings showed that the FCNN method demonstrated a high degree of accuracy, with the predicted outcomes exhibiting strong congruence with the actual production capacity distribution. This method, therefore, has substantial advantages in terms of precision and expediency.
3) Based on the optimized algorithm, production rates for Well XX-77-1 and Well XX-18-1 were predicted. The results demonstrated that the predicted values were closely aligned with the actual measured production data for each layer, indicating that the developed algorithm provides reliable predictions for single-phase oilwell production profiles under real-world operating conditions.

In this study, the researchers established a simplified forward model for predicting production well temperature profiles in wellbores, with the primary aim of verifying the feasibility of the intelligent interpretation method for multilayer commingled production under single-phase oil flow conditions. It should be noted that the current model is not applicable to multiphase flow scenarios, as the simplified physical framework does not account for the complex thermal and phase behavioral characteristics of such environments. This represents a key limitation of the present study. In the future, the researchers will focus on two main objectives: First, extending the physical forward model to incorporate multiphase flow mechanisms, and second, developing more advanced interpretation algorithms within an enhanced physical framework to further improve prediction accuracy across a wider range of production conditions.

Acknowledgements

This paper was supported by the Technology Cooperation project of the CNPC-SWPU Innovation Alliance (No. 2020CX030202) and the National Nature Science Foundation of China (No. 519042564).

Supplementary file

https://doi.org/10.46690/ager.2026.01.03

Conflicts of interest

The authors declare no competing interest.

References

Alan, C., Cinar, M., Onur, M. Prediction of production-inflow profile of a well producing single-phase flow of slightly compressible fluid from multilayer systems by temperature and/or pressure transient data. SPE Journal, 2024, 29(6): 3063-3090.

Alpaydin, E. Introduction to Machine Learning. MIT Press, Cambridge, USA, 2020.

Azimi, S., Britz, D., Engstler, M., et al. Advanced steel microstructural classification by deep learning methods. Scientific Reports, 2018, 1(1): 2128.

Cervantes, J., Garcia-Lamont, F., Rodríguez-Mazahua, L., et al. A comprehensive survey on support vector machine classification: Applications, challenges and trends. Neurocomputing, 2020, 408: 189-215.

Christos, K., Hicke, K., Krebber, K. Machine learning assisted BOFDA for simultaneous temperature and strain sensing in a standard optical fiber. Optics Express, 2023, 31(3): 5027-5041.

Denney, D. Intelligent-well completions in Agbami: Value added and execution performance. Journal of Petroleum Technology, 2010, 62(5): 49-51.

Ding, S., Su, C., Yu, J. An optimizing BP neural network algorithm based on genetic algorithm. Artificial Intelligence Review, 2011, 36(2): 153-162.

Ekechukwu, G. K., Sharma, J. Well-scale demonstration of distributed pressure sensing using fiber-optic DAS and DTS. Science Report, 2021, 11(1): 12505.

Gan, L., Dang, L., Wang, D., et al. Research on the processing and interpretation methods of distributed fiber optic

vibration signal logging injection profiles. Geoenergy Science and Engineering, 2024, 239: 212980.

Goodfellow, I., Bengio, Y., Courville, A., et al. Deep Learning. MIT Press, Cambridge, USA, 2016.

Hasan, A. R., Kabir, C. S., Lin, D. Analytic wellbore temperature model for transient gas-well testing. SPE Reservoir Evaluation and Engineering, 2005, 8(3): 240-247.

Hasan, A. R., Kabir, C. S., Wang, X. A. Robust steady-state model for flowing-fluid temperature in complex wells. SPE Production & Operations, 2009, 24(2): 269-276.

Hayden, G., Sharma, J. Machine-learning-assisted leak detection using distributed temperature and acoustic sensors. IEEE Sensors Journal, 2024, 24(2): 1520-1531.

Hui, G., Ren, Y., Bi, J., et al. Artificial intelligence applications and challenges in oil and gas exploration and development. Advances in Geo-Energy Research, 2025, 17(3): 178-183.

Jia, J., Li, D., Wang, L., et al. Novel transformer-based deep neural network for the prediction of post-refracturing production from oil well. Advances in Geo-Energy Research, 2024, 13(2): 119-131.

Kai, Z., Liang, W., Yong, D. DeepLog: Identify tight gas reservoir using multi-log signals by a fully convolutional network. IEEE Geoscience and Remote Sensing Letters, 2020, 17(4): 568-571.

Kokhanovskiy, A., Sakhno, D., Munkueva, Z., et al. A multicore fiber platform for distributed temperature sensing enhanced by machine learning algorithms. Optics and Laser Technology, 2025, 191: 113262.

Kumar, D., Chand, A., Masspoust, P. Approximation with fractal radial basis functions. Journal of Computational and Applied Mathematics, 2025, 454: 116200.

Lu, C., Qin, X., Sun, J., et al. Research progress and scientific challenges in the depressurization exploitation mechanism of clayey-silt natural gas hydrates in the northern South China Sea. Advances in Geo-Energy Research, 2023, 10(1): 14-20.

Ma, M., Huang, Z., Liao, Y., et al. Hybrid hyperplane gradient learning algorithm for RBF neural network. Neurocomputing, 2024, 587: 127626.

Ma, Y., Zhu, L. A review on dimension reduction. International Statistical Review, 2013, 81(1): 134-150.

Matinkia, M., Hashami, R., Mehrad, M., et al. Prediction of permeability from well logs using a new hybrid machine learning algorithm. Petroleum, 2023, 9(1): 108-123.

Milan, D., Vladimir, N., Danijela, D., et al. Review and statistical analysis of different global solar radiation sunshine models. Renewable and Sustainable Energy Reviews, 2015, 52: 1869-1880.

Mustafa, A., Elshafei, M., Al-Sarkhi, A. Artificial neural network application for multiphase flow patterns detection: A new approach. Journal of Petroleum Science & Engineering, 2016, 145(3): 548-564.

Obi, C., Hasan, A., Badejo, A., et al. Multiphase flow challenges in drilling, completions, and injection: Part 2. Petroleum, 2024, 10(4): 570-583.

Sagar, R., Doty, D. R., Schmldt, Z. Predicting temperature profiles in a flowing well. SPE Production Engineering, 1991, 6(4): 441-448.

Savitzky, A., Golay, M. Smoothing and differentiation of data by simplified least squares procedures. Analytical Chemistry, 1985, 57: 1477-1479.

Schmidhuber, J. Deep learning in neural networks: An overview. Neural Networks, 2015, 61(1): 85-117.

Shaban, H., Tavoularis, S. Measurement of gas and liquid flow rates in two-phase pipe flows by the application of machine learning techniques to differential pressure signals. International Journal of Multiphase Flow, 2014, 67: 106-117.

Shi, S., Liu, J., Li, M., et al. Research on numerical simulation and interpretation method of water injection well temperature field based on DTS. Processes, 2025, 13(1): 274.

Wang, M., Song, H., Li, M., et al. Prediction of split-phase flow of low-velocity oil-water two-phase flow based on PLS-SVR algorithm. Journal of Petroleum Science and Engineering, 2022, 212: 110257.

Wang, S., Zhang, N., Wu, L., et al. Wind speed forecasting based on the hybrid ensemble empirical mode decomposition and GA-BP neural network method. Renewable Energy, 2016, 94: 629-636.

Wei, M., Long, T., Duan, X., et al. Temperature response characteristics of the production profile for multilayered gas wells based on distributed temperature sensing monitoring. Journal of Energy Resources Technology, 2022, 144(12): 123002.

Wei, M., Zhou, J., Duan, Y., et al. Prediction of pressure and temperature profiles for two-phase flow in multilayered gas wells by DTS data. Geoenergy Science and Engineering, 2024, 234: 212615.

Zhang, D., Chen, Y., Meng, J. Synthetic well logs generation via recurrent neural networks. Petroleum Exploration and Development, 2018, 45(4): 629-639.

Zhou, H., Liu, J., Fei, J., et al. A model based on the random forest algorithm that predicts the total oil-water two-phase flow rate in horizontal shale oil wells. Processes, 2023, 11(8): 2346.